

Micro-Precision Interferometer Testbed: First Stabilized Stellar Fringes

Gregory W. Neat, John F. O'Brien, Noble M. Nerheim, Robert J. Calvet,
Harjit Singh, and Stuart Shaklan

Jet Propulsion Laboratory, California Institute of Technology, Pasadena, CA

ABSTRACT

This paper presents initial results that demonstrate the end-to-end operation of the Micro-Precision Interferometer (MPI) testbed. The testbed is a full-scale model of a future space-based interferometer, containing all the spacecraft and support systems necessary to perform an astrometric measurement. The primary objective of the testbed is to provide an end-to-end problem to evaluate and integrate new interferometer technologies, such as vibration isolation, structural quieting, active optics, and metrology systems. This paper shows initial testbed functionality in terms of the ultimate performance metric: stabilization of stellar fringes (from a pseudo star). The present incarnation of the evolving testbed uses a fringe tracker and pointing control subsystem to stabilize the fringe position to the 72 nm (1 σ MS) level in the presence of the ambient laboratory seismic noise environment which is a factor of 10 higher than that expected on-orbit. These encouraging preliminary results confirm that the MPI testbed provides an essential link between the extensive ongoing ground-based interferometer technology development activities and the technology needs of future spaceborne interferometers.

Key Words: Micro-Precision Interferometer testbed, Michelson interferometer, vibration attenuation, fringe tracker, pointing control, wave tilt control

1. INTRODUCTION

For the last several years, the Jet Propulsion Laboratory (JPL) Control Structures Interaction (CSI) Program has been developing new vibration attenuation technologies required by future precision optical space missions. This effort originated by identifying the need for such technologies as a result of deriving the requirements for the Focus Mission Interferometer¹ (FMI); a space-based, 30 m baseline, partial aperture telescope. The control approach evolved from the ensuing FMI conceptual design. Figure 1 presents the fundamental approach in terms of the three vibration attenuation layers; vibration isolation, structural quieting, and active optics. The basic strategy, referred to as the "layered" control approach, is to isolate vibrating machinery at the point of attachment, damp specific undesirable structural modes that limit optical control system bandwidths, and finally to actively control specific optical elements to achieve the desired optical performance. This paper focuses primarily on the CSI Program's latest advancements in the active optics layer.

The CSI Phase B testbed provided the first hardware validation of the layered control strategy. The goal for this 3 m cantilevered truss structure was to stabilize an optical pathlength to the nanometer-level in the presence of a single-axis shaker input disturbance using a single-axis vibration isolation stage, a number of active and passive structural damping struts, and an active optical delay line. The results indicated a factor of 5000 attenuation from input disturbance to output optical pathlength, with output variations on the order of 5 nm (RMS)². The next logical step was to validate the layered control approach in hardware on a complete end-to-end instrument. This led to the design and assembly of the Micro-Precision Interferometer (MPI) testbed³.

The MPI testbed is a ground-based, suspended hardware model of a future space-based interferometer located

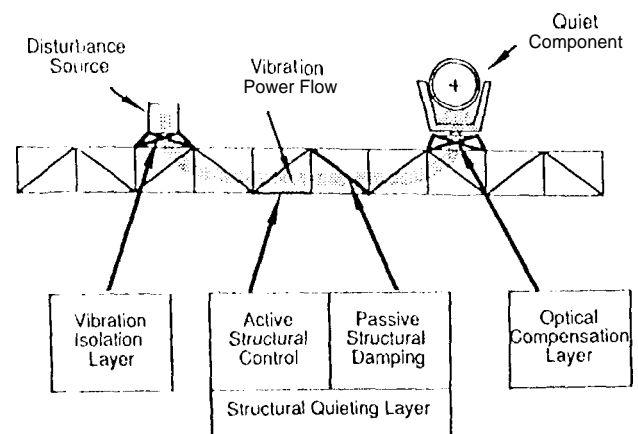


Figure 1. The CSI "layered" control approach.

at JPL. The primary objective of the testbed is to perform the system integration of CSI technologies required to demonstrate the end-to-end operation of a space-based interferometer. In addition, the testbed allows benchmark comparisons of competing control technologies (e.g., 6-axis isolation systems) under similar conditions, using a realistic optical performance metric.

Figure 2 shows how the testbed provides a critical link between ground-based interferometry and future space-based interferometry missions. The optical design evolved from a ground-based operational interferometer (Mark III) which is bolted to bed rock on the summit of Mt. Wilson⁴. The design and integration of the complex optical system with a large, lightly damped flexible structure draws heavily from the CSI Phase B experience with regard to control structure interaction issues. The testbed dimensionally and dynamically is representative of a number of future interferometer missions that are presently at the conceptual design phase. Two future interferometer mission concepts that will benefit directly from this effort will be the Orbiting Stellar Interferometer (OSI)⁵ and the Precision Optical Interferometer in Space (POINTS)⁶. The testbed can address different interferometry mission needs by reconfiguring the relative location between the disturbance sources and the quiet optical components. This paper focuses on the configuration representative of the OSI mission.

OSI is a mission concept for a first-generation space interferometer with astrometric and imaging goals. The approach uses three collinear Michelson interferometers, each defined by a pair of collecting apertures or siderostats, to perform μ arcsec-level astrometric measurements and milliarcsec-level imaging of the heavens. Rather than depend on accurate base body pointing of the entire spacecraft as with full aperture systems (e.g., HST) this design utilizes high bandwidth optical sensing (metrology systems) and high bandwidth control of optical elements to

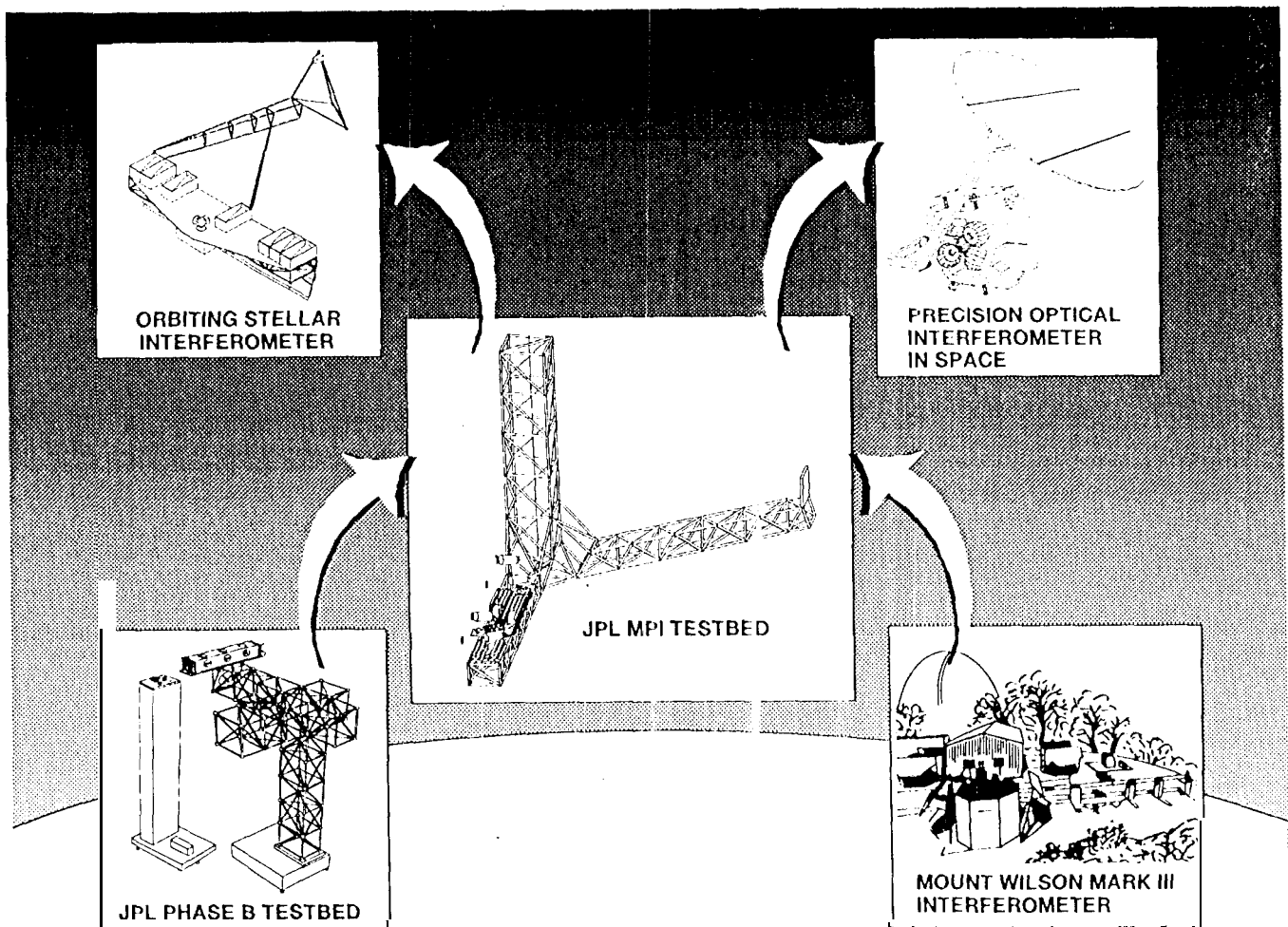


Figure 2. The role of MPI in the spaceborne interferometry technology development process.

achieve precision pointing requirements. End-to-end instrument astrometric performance depends on four factors: (1) the number of photons, (2) the instrument's effective collecting aperture diameter, (3) the instrument's ability to suppress vibrations of critical optical elements, and (4) relating the measurements from the three interferometers to one another. This paper focuses primarily on (3). Instrument design ultimately is a trade-off between maximizing baseline length (2) and creating a vibration attenuation (3) and the sensing (4) challenge that is solvable.

Figure 3 shows a schematic diagram of a single Michelson interferometer observing a stellar source. The active optical layer contributes significantly to the bottom-line vibration attenuation challenge: stabilize and measure the stellar fringe position down to the 10-nanometer (RMS) level. Fringe stabilization to this level implies the light path from the star, through one arm of the interferometer (S, 1, 2, 3, 4, 5, 6, 7, 8, 9 in Figure 3) equals the light path from the star, through the other arm of the interferometer (S, 1', 2', 3', 4', 5', 6', 7', 8', 9' in Figure 3). Stabilization of the resulting interference pattern at the beam combiner (component 9 in Figure 3) requires successful operation of two optical subsystems: the pointing control subsystem and the fringe tracking subsystem. The pointing control subsystem independently points each interferometer arm at the same target star by articulating the respective siderostat (1 or 1') and fast steering mirror (4 or 4') based on the two stellar images from the pointing camera. Once each interferometer arm is "looking" at the same star, the fringe detector (see Figure 3) can measure stellar fringe position. The fringe tracking subsystem stabilizes the fringe position in the presence of spacecraft disturbances and rigid body motion. The fringe tracker subsystem has a single actuator in one of the interferometer arms which is the high bandwidth, high dynamic range active delay line (5, 6, 7 in Figure 3). This actuator translates linearly, introducing an optical path delay, as commanded by the fringe detector, in order to equalize the two optical paths.

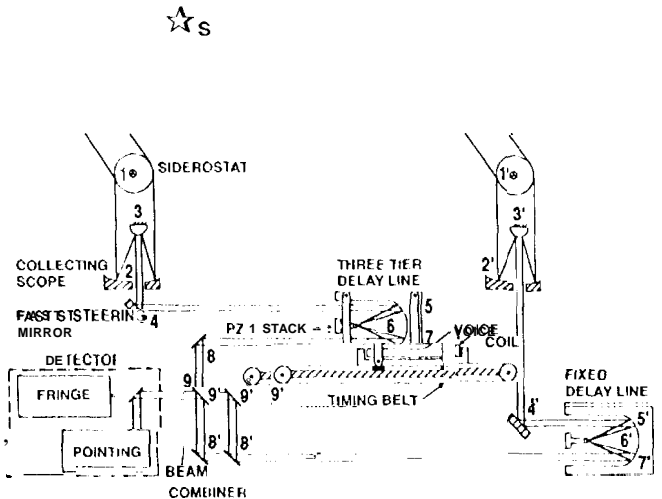


Figure 3. Stellar optical path for a Michelson interferometer.

Each of the three colinear OS1 interferometers stabilizes the stellar fringes of a specific star. Two interferometers (guide interferometers) stabilize the fringes of bright target stars. These interferometers provide a high bandwidth, μarcsec -level measurement of the attitude of the instrument's colinear baselines. The bright target stars provide ample signal level for the guide interferometer pathlength and pointing control subsystems. The third interferometer (science interferometer) observes the dim science object. A complex laser metrology system^{8,9} relates the measurements from the three interferometers to one another at the nanometer level. The spacecraft contains two metrology systems: an internal system to monitor internal pathlength changes (from the collecting aperture-1, 1', to the beam combiner-9 in Figure 3) and an external system to measure flexible body motions of the three baselines relative to one another. The high sensing bandwidths provided by the laser metrology system and the two guide interferometers produce the feedback signal for the path length and pointing control subsystem actuators of the science interferometer.

The MPI testbed is dimensionally a full-scale model of OS1. The testbed contains all the necessary systems to perform a space-based astrometric measurement. These systems include a 7 m x 7 m x 6.5 m softly suspended truss structure with the necessary mounting plates for subsystem hardware, a six-axis vibration isolation system which supports a reaction wheel assembly to provide a flight-like input disturbance source, a complete Michelson interferometer, internal and external metrology systems, and a star simulator that injects the stellar signal into the interferometer collecting apertures. This paper emphasizes the operation of the Michelson interferometer which functions as a guide interferometer. Figure 4 compares the present MPI configuration with the OS1 mission concept in terms of top-level system parameters and requirements. The only major difference in top-level requirements is the pointing stability. This is because the collecting aperture diameter for OS1 is a factor of 10 greater than the collecting aperture diameter for MPI (30 cm, 30 mm, respectively).

A number of system parameters make the stabilization of stellar fringes in the ground-based laboratory more challenging than on-orbit. The attitude of the MPI testbed, which is determined by a passive three-point suspension system, can vary as much as a few degrees from day to day compared with the arcmin accuracy of the OSI basebody control system. In addition, the MPI disturbance environment has an additional contribution from the ambient lab seismic vibrations. As shown in the results section, the ambient variation in stellar fringe position is a factor of 10 greater than that expected on-orbit (-10 pm vs. -1 pm). The major contributors to this motion are the rigid body oscillations of the structure and motion of the star simulator which sits on the lab floor. The majority of this energy is below 1 Hz. This paper addresses the problem of stabilizing stellar fringe position in the presence of this ambient laboratory noise environment.

2. TESTBED CONFIGURATION

Figure 5 shows a bird's-eye view of the MPI testbed. The six-axis isolation system, located at the base of the tower, isolates the testbed's reaction wheel disturbances from the truss structure. The optics boom contains all the interferometer optical components and will be the focus of the remainder of the paper. The interferometer observes a pseudo star that resides on a 4-m optics table situated parallel to the optics boom. Finally, the external metrology boom supports the metrology hardware necessary to measure the relative position (in three dimensions) of the interferometer baselines. This will become important when the second baseline is added to the testbed.

Figure 6 zooms in on the optics boom and traces the stellar optical path through the star simulator and testbed optical train. The included schematic diagram of the same region calls out important optical components. In addition, the inset in Figure 6 indicates the changes in the stellar beam cross section at the respective locations along the optical path. The following discussion traces the stellar optical path through the system. For further details on the optical system, see reference 10.

The "star" source is the laser head of a commercial laser interferometer system that sits on a pneumatically suspended optical table. The laser output is a 6-mm-diameter beam with two orthogonally polarized beams that differ in frequency by 1.8 MHz. The beam diameter is expanded to 30 mm and then divided by a polarization-sensitive beamsplitter. A number of fold mirrors direct each of the two polarization-specific beams to a final fold mirror located near the respective interferometer collecting aperture location. The final fold mirror, which directs the stellar beam from the table to the MPI structure, is mounted on a support that overhangs the suspended structure, to provide vertical feed to the siderostat.

	MICRO-PRECISION INTERFEROMETER TESTBED	ORBITING STELLAR INTERFEROMETER
FUNCTIONS	ASTROMETRY	ASTROMETRY & IMAGING
SIZE	7 m	7 m
# INTERFEROMETER BASELINES	1 (GUIDE)	3 (2 GUIDE, 1 SCIENCE)
RIGID BODY CONTROL	PASSIVE SUSPENSION SYSTEM (1-DEGREE ACCURACY)	SC ACS (1-ARCMIN ACCURACY)
STELLAR SOURCES	(SIMULATED) HE NE LASER	MAGNITUDE 7 TO 20 (WHITE LIGHT)
DISTURBANCE ENVIRONMENT	1 MAGELLAN FLIGHT SPARE RWA + AMBIENT SEISMIC VIBRATIONS (10 μm (RMS))	4 HST CLASS RWAS (1 μm (RMS))
MASS	400 kg	1728 kg
FRINGE VISIBILITY	0.7	0.7
FRINGE STABILITY	10 nm (RMS)	10 nm (RMS)
COHERENCE TIME (GUIDE)	-1 hr	-1 hr
POINTING STABILITY	0.7 arcsec	0.03 arcsec

Figure 4. Top-level system parameters and requirements comparison between MPI and OSI.

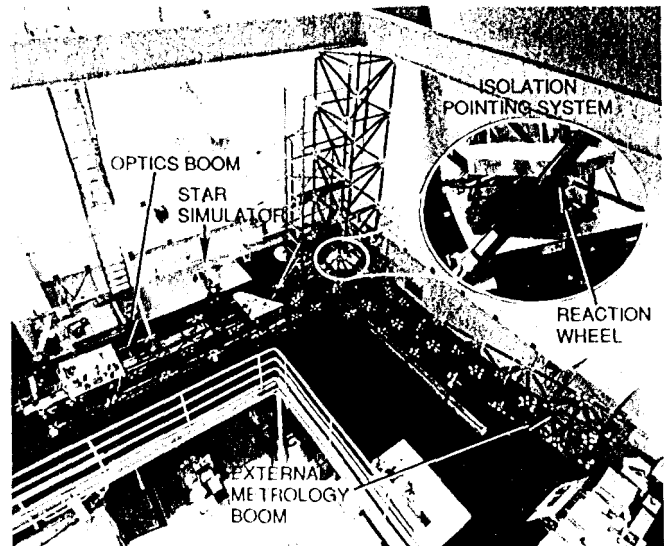


Figure 5. Bird's-eye view of the MPI testbed.

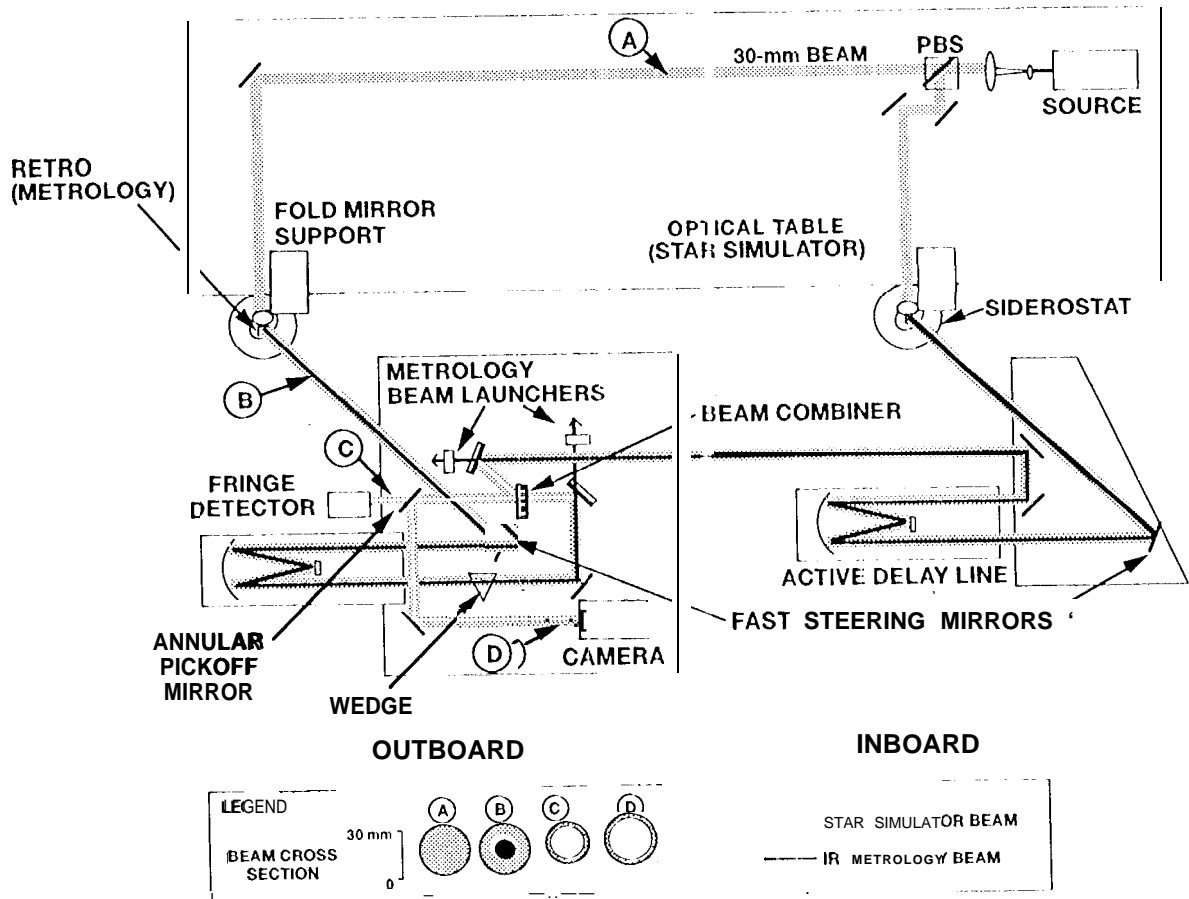
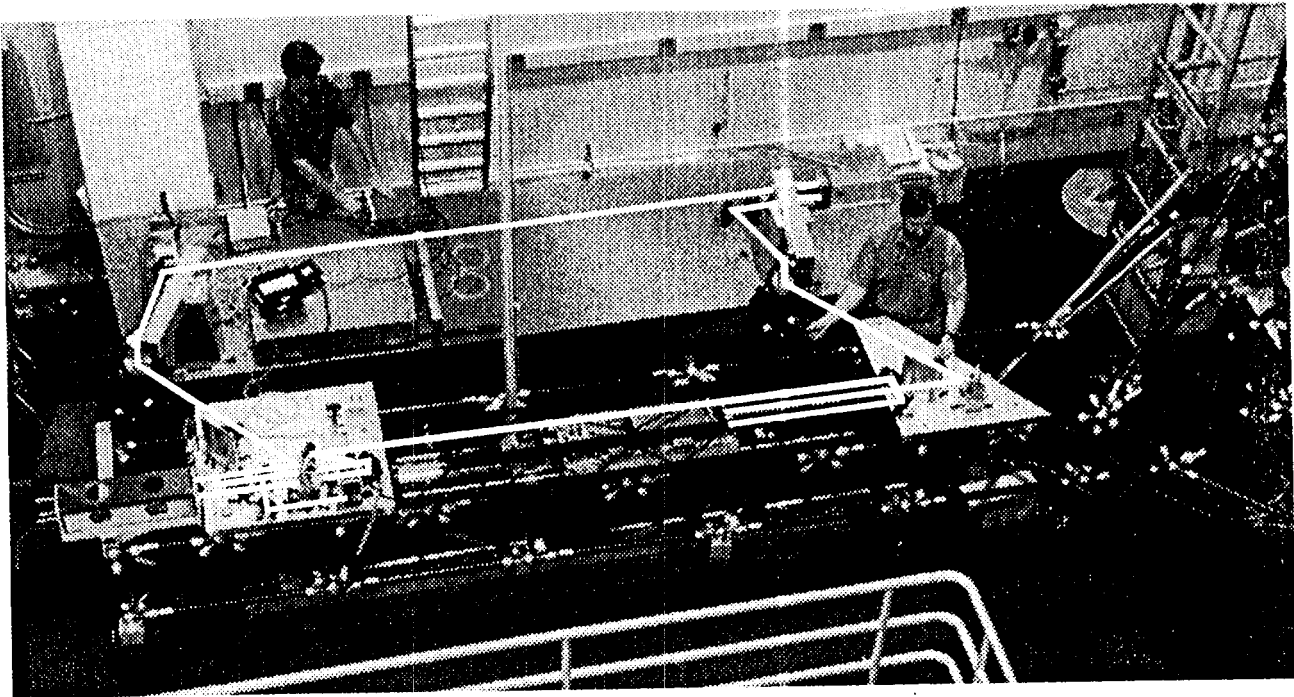


Figure 6. optical layout of the first MPI baseline from star simulator to optical detectors. The schematic diagram and photo depict the same region of the testbed. The inset shows the beam cross section at different points in the optical path.

The two interferometer beam paths experience symmetrical reflections in the two interferometer arms on the testbed. The following traces the "inboard" beam path (collecting aperture on the right-hand side of the figure) without loss of generality. The two-axis gimbaled siderostat mirror contains a 12-mm-diameter retroreflector used by the internal metrology system. Therefore, the beam leaving the siderostat consists of an annular stellar beam and a central infrared metrology beam. A 90/10 beam splitter picks off 10% of this beam and sends it to a coarse acquisition sensor, used by the siderostat to initially acquire the star. The remaining light travels to the 2-axis, high bandwidth fast steering mirror which sends the light into the active delay line.

The output beam from the active delay line reflects off three fold mirrors, sending the beam to the "outboard" plate (closest to the collecting aperture on the left-hand side). The third fold mirror directs the beam to the beam combiner where the beam from the inboard siderostat is reflected to join the transmitted beam from the outboard siderostat. After the beam combiner, the central region of the combined stellar beams passes through the hole in the annular pickoff mirror to a fringe detector as a single beam with two orthogonal components with frequencies that differ by 1.8 MHz and phase that depends on the optical path of each. The detector, a standard receiver for the commercial interferometer, produces a 1.8 MHz heterodyne signal with a phase that varies as the OPD of the stellar beams changes. The annular pick-off mirror reflects the outer region (30-mm OD and 25-mm ID) of each stellar beam and directs them to a CCD camera.

In addition to the stellar beam, two independent internal metrology beams trace the internal paths (from beam combiner to siderostat corner cube) of each interferometer arm. In contrast to the visible stellar beam, the internal infrared metrology system is a two-pass system. Beam launchers, in close proximity to the beam combiner, inject the respective metrology beams into the system through holes bored in neighboring fold mirrors.

Finally, the outboard optical path has an additional 1-arc-minute annular wedge that contains a central hole that corresponds to the pick-off mirror hole diameter. This causes the outer annular region of the beam from the outboard siderostat to be offset by 1 arc minute while the center portion passes through undeviated. Thus, at the pick-off mirror, the central portions of the two beams are parallel while the outer regions diverge at an angle of 1 arc minute. The two reflected annuli are brought to a focus on the CCD camera. The wedge therefore enables a simple means to sense wave tilt error in the optical system with a single sensor.

3. POINTING CONTROL SUBSYSTEM

The purpose of the pointing control subsystem is to ensure that each arm of the interferometer points at the same target star. Equivalently, this subsystem guarantees the wave fronts from the two collecting apertures are parallel. Achieving this function is a necessary prerequisite to stabilizing stellar fringes. The MPI pointing subsystem must stabilize the stellar centroid position to a small fraction of the diffraction limit of the imaged spot. The pointing requirement is therefore $(\lambda/30\text{mm}) \cdot I = 2.1 \mu\text{rads}$. Since each arm of the interferometer must independently "point", each arm has a stand alone pointing control subsystem. Figure 7 shows the pointing control subsystem for one arm.

This subsystem has two actuators: the low-bandwidth, large-angle siderostat, and the high-bandwidth, precise, fast steering mirror. As in the case of the eventual OS1 mission, the main function of the MPI siderostat is to acquire the star. Once acquired, the siderostat is locked down during the observation period. Therefore, the fast steering

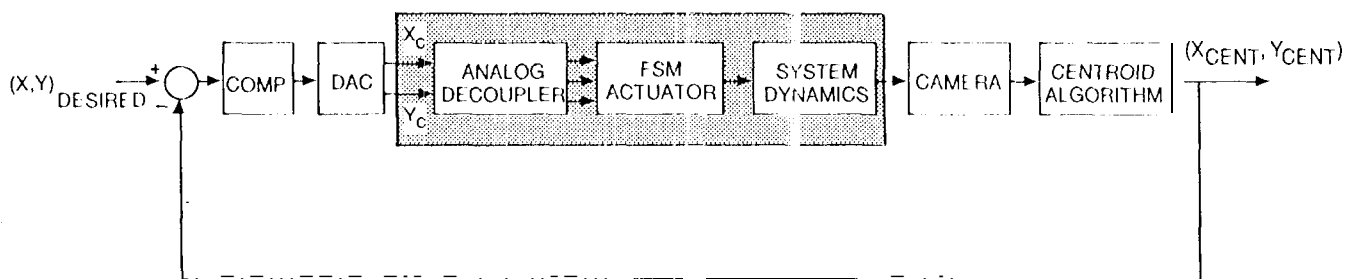


Figure 7. Block diagram of the pointing control subsystem. The shaded regions indicate the analog components.

mirrors are the pointing control subsystem disturbance rejection actuators. The MPI high voltage fast steering mirror has a bandwidth of 1 kHz and an angular range of ± 35 arcsecs. Three symmetrically orientated piezo actuators position the mirror, providing tip and tilt motion.

The sensor for the pointing control subsystem is a high-frame-rate 32×32 pixel CCD camera. The camera screen is divided in half so that each arm of the interferometer has an assigned region on the camera to be imaged. This is possible due to the annular wedge discussed in Figure 6. During closed loop operation, only a 5×5 pixel window is transferred from the camera to the processor enabling high sample rates. The dedicated processor for this loop calculates x , y centroid values for this 5×5 image at 4 kHz.

The control loops to maintain the desired x and y centroid position are completely decoupled over the frequency range of interest. For this initial effort, the compensator is a simple first-order low-pass filter. The unity gain frequency for the loop (both axes) is 30 Hz. The digitally implemented compensator spits out an x and y command signal to an analog decoupling circuit, which transforms the (X_c, y_c) command signals into three drive voltages for the fast steering mirror.

All four loops (inboard x , y , outboard x , y) have the same compensator. Over the dc-30Hz frequency range, the total loop transfer functions for these loops are identical. When these bandwidths increase with the introduction of the reaction wheel disturbance, this will probably not be true.

Figure 8 shows an open loop power spectral density of the outboard y centroid position in response to the lab ambient environment. Note that the majority of the energy is below 1 Hz due to the rigid body modes of the suspended truss and the motion of the star simulator table. The plot also indicates the ambient disturbance level drops below the camera noise floor above 10 Hz. For this data set, the total open loop spot motion is $.747 \mu\text{rad}$ (RMS) which is below the required pointing stability. This suggests the pointing control subsystem is not necessary to reject the ambient disturbance environment. However, rigid body testbed motion over long time periods (i.e., hours) easily introduces enough pointing error to justify the closed loop system.

Figure 9 shows the results of a pointing control subsystem experiment. Between $t = 0$ to 7 seconds, the plot shows ambient disturbances which include a moving star (~ 1 Hz), a swaying structure (~ 1 Hz), air conditioning unit vibrations (~ 30 Hz) . . . However, at $t = 7$ seconds, the loops are closed and the centroid position locks to the desired 15.8 pixel set point position, rejecting all disturbances. The pointing control subsystem improved angular stability

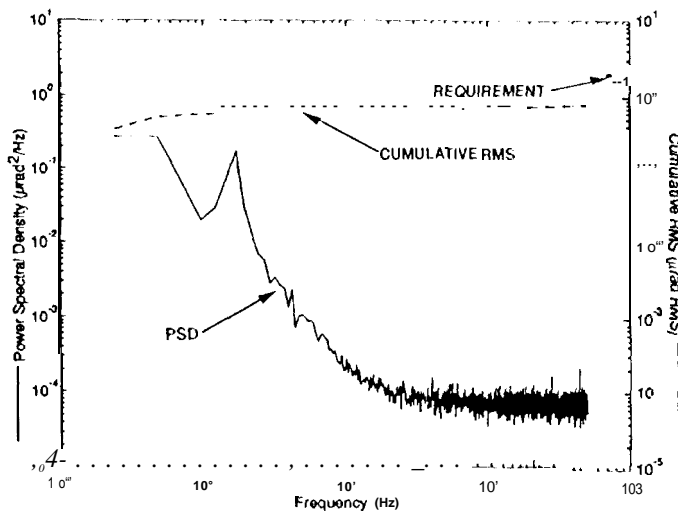


Figure 8. Power spectral density of the outboard y -axis centroid motion in response to the ambient disturbance environment. The dashed line indicates the cumulative RMS.

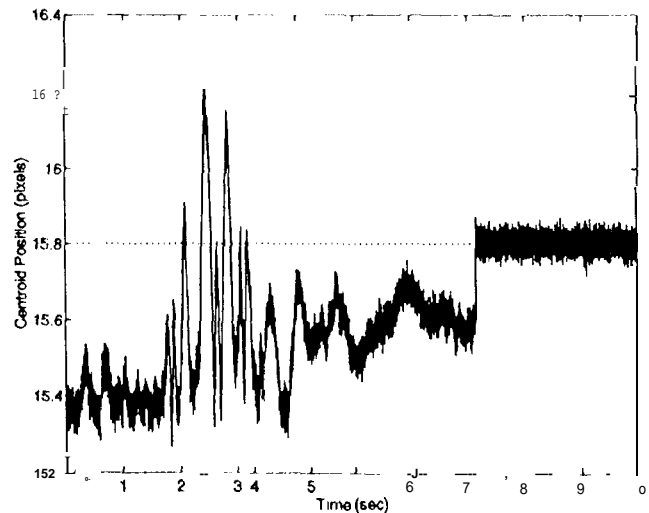


Figure 9. Plot of the inboard y -axis centroid position over a ten second period. The pointing control subsystem is open loop from $t = 0$ to $t = 7$ seconds. At $t = 7$ seconds, the pointing loop is closed. The set point is 15.8 pixels.

from 2.35 μrad (RMS) open loop, to .27 μrad (RMS) closed loop. With the two interferometer arms locked onto the same star, the fringe tracker subsystem can now function.

4. FRINGE TRACKING SUBSYSTEM

The purpose of the fringe tracking subsystem is to equalize stellar pathlength from the target star through each arm of the interferometer to the point they are combined. The MPI fringe tracking subsystem (and the OS1 subsystem) must stabilize the optical path difference in the two arms or equivalently the stellar fringe position down to 10 nm (RMS). This subsystem consists of two nested closed loops stems, each with a dedicated sensor and each using the same actuator in a different manner. Figure 10 shows a block diagram of MPI's fringe tracking subsystem.

The "inner" loop is also referred to as the internal path length control subsystem. The purpose of this loop is to precisely maintain the desired optical delay as commanded by the fringe tracker (outer loop). The actuator for this subsystem is the active delay line which actually consists of three nested actuators. This three-tiered actuator acts as a linearly translating retroreflector with tremendous dynamic range. A stepper motor provides low frequency, long travel capability (m). An intermediate voice coil actuator translates (cm) the entire cat's-eye assembly in the mid-frequency range (dc -100 Hz). A reactuate piezo supporting the secondary mirror provides the high bandwidth (kHz) precise actuation stage (μm). Analogous to the siderostat actuator of the pointing control subsystem, the coarse stepper motor is used primarily to slew and acquire a new stellar fringe. Once acquired, this stage is locked down and the other two stages provide the actuation necessary to reject disturbances during an observation.

The sensor for the inner loop is the IR metrology system, used to monitor internal pathlength changes from the beam combiner to the respective siderostat mounted corner cubes (see Figure 6). With the custom electronics, this two-pass system can measure the relative delay line position to within 2.5 nm. The inherently digital laser counter board provides internal pathlength updates at 8 kHz to the dedicated pathlength control processor. This processor implements the fourth-order pzt and fourth-order voice coil compensators which have bandwidths of 650 Hz and 100 Hz, respectively. This processor spits out two command signals to the active delay line: one to the voice coil and one to the pzt.

The outer loop or fringe tracker looks at the inner loop as an extremely precise, high-dynamic range, high-bandwidth actuator (see Figure 10). The sensor for this loop is the fringe detector. The planned OS1 system views white light sources which have a unique central fringe. In contrast, the MPI star uses a visible laser which repeats every 633 nm. With respect to acquiring the stellar fringe and sensing its position, the white light source requires modulation of the active delay line to enable measuring fringe amplitude and phase. This adds additional complexity

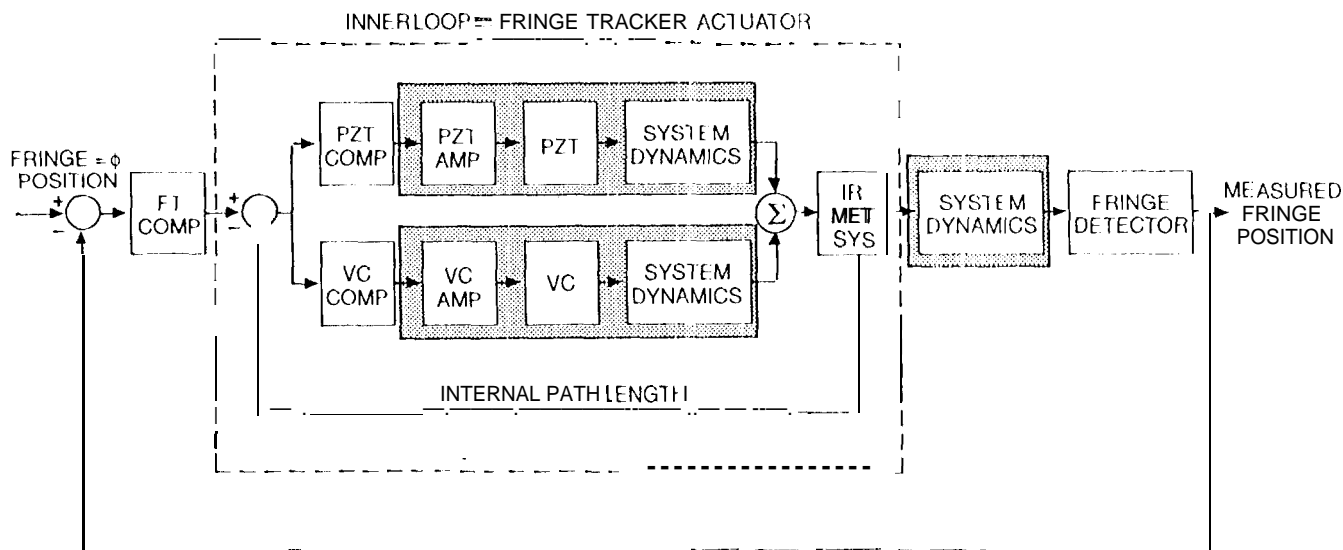


Figure 10. Block diagram of the fringe tracker subsystem. The shaded regions indicate the analog components.

to the fringe tracker sensor and actuator compared to that required by the present MPI visible heterodyne system. This system references all fringe motion to the position at the time the fringe tracker began measuring fringes and calls that the central fringe. All subsequent optical path difference variations are with respect to this initial measured position. It is important to note that this simplified fringe tracking system does not change the disturbance rejection approach to stabilizing stellar fringes.

The MPI fringe detector provides fringe position measurements at 8 kHz. These measurements are difference with the desired fringe position (0) to create the error signal to be filtered by the fringe tracker compensator. The bandwidth of the fringe tracking loop is 100 Hz. The compensator is a simple first-order low-pass filter implemented on a dedicated fringe tracker processor. The output of this filter is the command signal to inner loop.

Figure 11 shows an open loop power spectral density of MPI fringe position in response to the lab ambient environment. Note that the majority of the energy is below 1 Hz due to the rigid body modes of the suspended truss and the motion of the star simulator table. The ambient fringe motion is $5.66 \mu\text{m}$ (1 MS) which violates the 10 nm (RMS) by a factor of 500. Simulation studies of future spaceborne interferometer missions predict the open loop fringe motion to be on the order of $1 \mu\text{m}$ (RMS)¹. Therefore, in order to achieve the 10 nm (RMS) attenuation level in this noisy ground-based laboratory (see Figure 11), the fringe tracking subsystem must have significant disturbance rejection ability at low frequency.

Figure 12 shows measured fringe position under three different conditions. The first 22 seconds shows the open loop response to the lab ambient disturbances. The open loop motion is $10 \mu\text{m}$ (RMS). Between 22 and 37 seconds, the inner loop was closed on its own. Note that in this configuration (with the outer loop open) the inner loop maintains a constant internal path length. Thus, the instrument looks like a rigid structure from the fringe detector perspective. This configuration removes all fringe position motion that results from the resonant structure but still has fringe position motion from many other sources: rigid body motion of the structure, static deformation of the floor (and therefore change in star position), atmospheric disturbances and dynamics of the optics table. All of these factors can be seen in this time period. At $t = 37$ seconds, the outer loop was closed. In this configuration, the fringe tracker subsystem stabilizes fringe position to 72 nm (RMS) in the presence of the lab ambient disturbances.

5. TRANSFER FUNCTION RESULTS

Although the dominant vibration source for spaceborne interferometers is from the spacecraft reaction wheels, which are characteristically narrow-band in nature, a convenient means of assessing disturbance rejection is

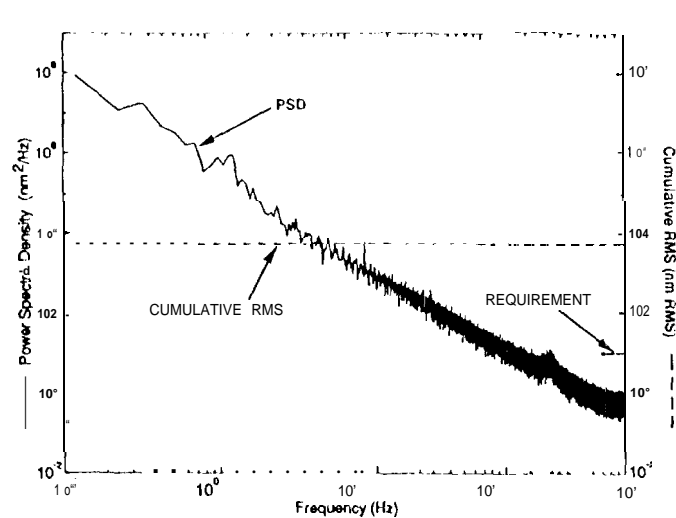


Figure 11. Power spectral density of the fringe position in response to the ambient disturbance environment. The dashed line indicates the cumulative RMS.

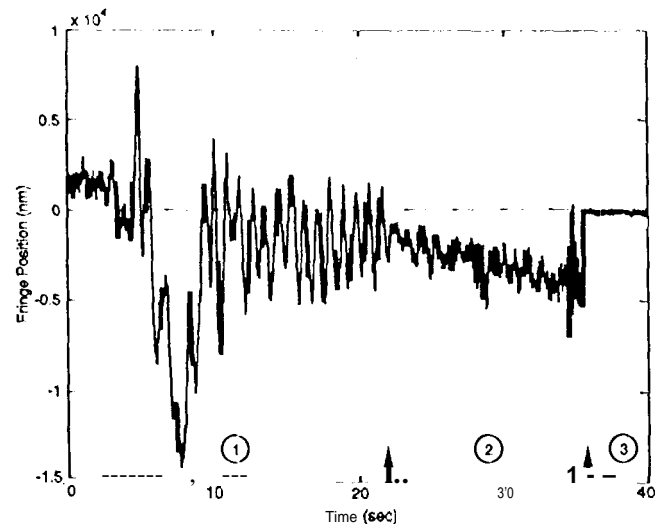


Figure 12. Plot of fringe position versus time under three different fringe tracker configurations: (1) open loop, (2) inner loop closed, (3) inner and outer loop closed. The set point is 0 nm.

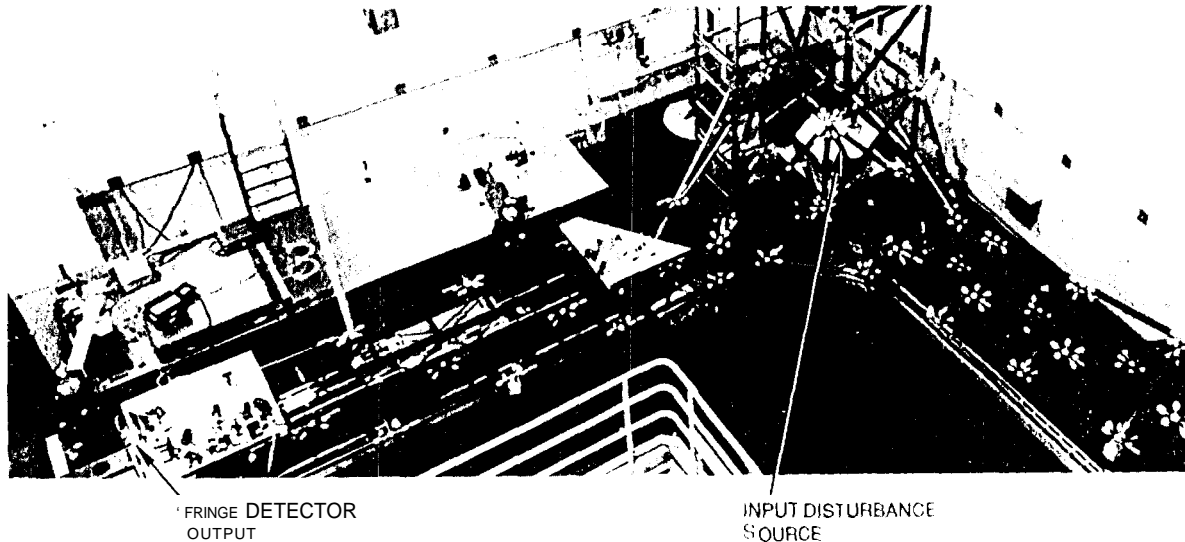


Figure 13. Relation between the shaker disturbance input location (collocated with the reaction wheel) and the fringe detector output location.

measuring a broad-band transfer function from disturbance input to sensor output. Figure 13 shows the shaker input mounting location (collocated with the reaction wheel) and the fringe detector output location used for these measurements. Figure 14 shows the open loop transfer function. Each of the vibration attenuation technologies targets a different frequency range with the collective goal of reducing the entire transfer function (see dashed line in Figure 14). This corresponds to shaker (or equivalently reaction wheel) disturbances not being measurable at the fringe detector.

Figure 15 compares the open loop transfer function with the transfer function measured with an operational pointing control subsystem and fringe tracker subsystem. Note the significant amount of attenuation at low frequency. The fringe tracker loses its effectiveness around 100 Hz (the unity gain frequency for this subsystem).

Finally, Figure 16 shows initial results from the combination of two technology layers: active optics and active/passive 6-axis vibration isolation. The same transfer function was measured with an operational six-axis vibration isolation system^{7,12} and the active optical system from Figure 15. This initial measurement shows how these two layers complement each other. In the low-frequency region, all the disturbance rejection comes from active optics. Both layers contribute to the vibration attenuation in the 10 -100 Hz frequency range. Beyond the bandwidth of the active optics (100 Hz) all the disturbance rejection is due to the vibration isolation system.

6. FUTURE WORK

The end-to-end performance of the MPI testbed continually improves. At submission time of this paper, the stability of the closed loop fringe position improved from 72-rim (RMS) to 26 nm (RMS) by tuning a few of the compensator designs. This will continue until the 10 nm (RMS) requirement is demonstrated with the vibrating reaction wheel.

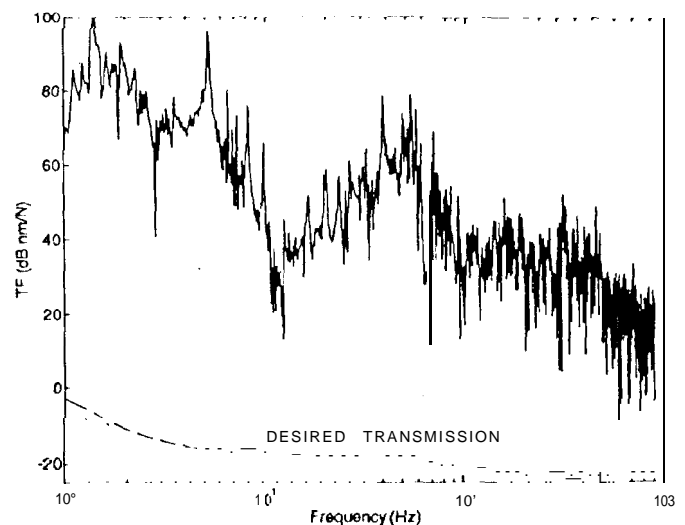


Figure 14. Open loop transfer function between shaker input force (N) and fringe position output (rim). The dashed curve indicates an approximate desired shape of this curve after the application of vibration attenuation technologies.

The next major configuration change to the evolving MPI testbed will be the addition of a second interferometer baseline. This will enable the evaluation of the feed-forward strategy to pointing a science interferometer, using attitude information from the guide interferometer and the metrology systems. In the near term, the star simulator may be upgraded to a white light source. This would require the corresponding upgrade in the fringe detector.

Finally, these encouraging preliminary results confirm that the MPI testbed provides an essential link between the extensive ongoing ground-based interferometer technology development activities and the technology needs of future spaceborne interferometers. The most immediate prospect for a spaceborne interferometer is the Stellar Interferometer Metrology Experiment (SITE)¹³ presently under evaluation for the In-Space Technology Experiment Program (In-STEP). SITE proposes to fly a single Michelson interferometer in the cargo bay of the Shuttle. The dimensions, component count, vibration attenuation challenge, and technical approach are extremely similar to the MPI system.

7. ACKNOWLEDGMENTS

The research described was performed at the Jet Propulsion Laboratory, California Institute of Technology, under a contract with the National Aeronautics and Space Administration. The author would like to thank the entire MPI team for their efforts. The author would also like to thank the leader of the CSI Program, Bob Laskin, for his technical and financial support.

8. REFERENCES

1. R.A. Laskin, and M. San Martin, "Control/Structure System Design of a Spaceborne Optical Interferometer," Proceedings of the AAS/AIAA Astrodynamics Specialist Conference, Stowe VT, 1989.
2. J.P. Spanos, Z. Rahnman, C. Chu, and J.F. O'Brien, "Control Structure interaction in Long Baseline Space Interferometers," 12th IFAC Symposium on Automatic Control in Aerospace, Ottobrunn, Germany, September 7-11, 1992.
3. G.W. Neat, L.F. Sword, B.E. Hines, and R.J. Calvet, "Micro-1 Precision Interferometer Testbed: End-to-End System Integration of Control Structure Interaction Technologies," Proceedings of the SPIE Symposium on OE/Aerospace, Science and Sensing, Conference on Spaceborne Interferometry, vol. 1947, pp 91-103, Orlando, FL, 1993.
4. M. Shao, M.M. Colavita, B.E. Hines, D.H. Staelin, D.J. Hutter, K.J. Johnston, D. Mozurkewich, R.S. Simon, J.I. Hersey, J.A. Hughes, and G.H. Kaplan, "Mark III Stellar Interferometer," *Astron. Astrophys.* 193, 357-371, 1988.

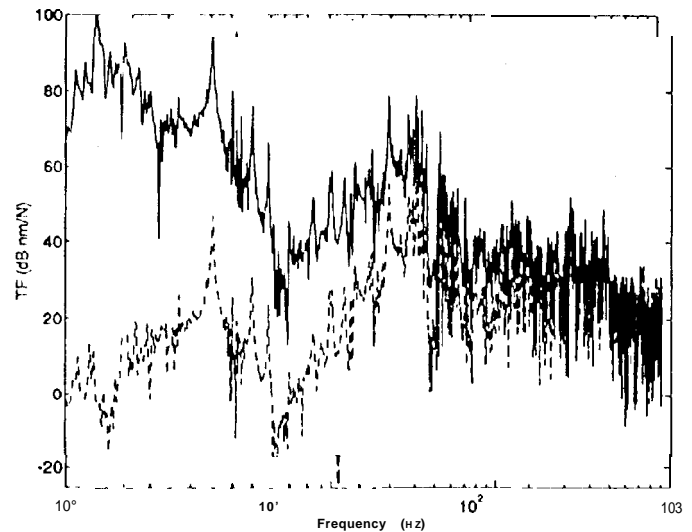


Figure 1.1. Comparison of the open loop transfer function (solid) between shaker input force (N) and fringe position output (nm) and the same transfer function (dashed) with the pointing and fringe tracker subsystems operational.

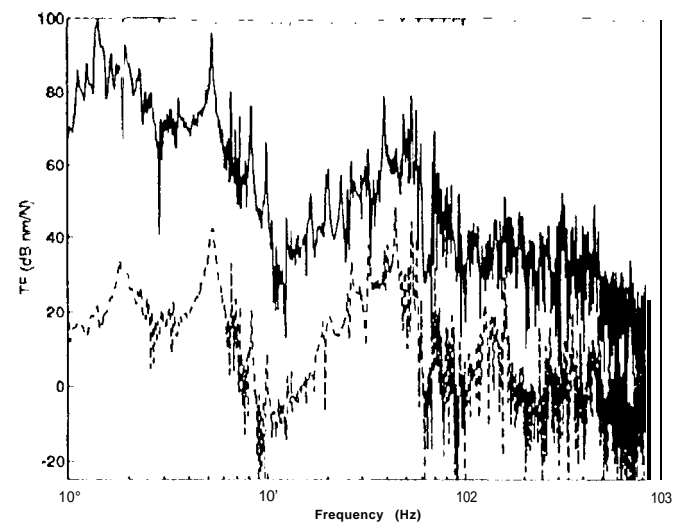


Figure 1.2. Comparison of the open loop transfer function (solid) between shaker input force (N) and fringe position output (nm) and the same transfer function (dashed) with the optical systems and the six-axis vibration isolation system operational.

5. M.M.Colavita, M. Shao, M.D. Rayman, "OS1: Orbiting Stellar interferometer for Astrometry and Imaging," Applied Optics, Special Section on the Williamsburg Space Optics Conference, 1991.
6. R.D.Reasenberg, et. al. "Microarcsec Optical Astrometry: An Instrument and its Astrophysical Applications," Astronomical Journal, 96, pp. 1731-1745, Nov. 1988.
7. J.F. O'Brien, G.W. Neat, J.W. Melody, R.J. Calvet, and A.v. Flotow, "Six-Axis Vibration Isolation System for Spaceborne Interferometers," Proceedings of the SPIE International Symposium on AeroSense, Conference on Spaceborne Interferometry II, vol. 2477, Orlando, FL, April 1995.
8. Y. Gursel, "Laser metrology gauges for OS1," Proceedings of the SPIE Symposium on OE/Aerospace, Science and Sensing, Conference on Spaceborne Interferometry, vol. 1947, pp. 188-197, Orlando, FL, April 1993.
9. Y. Gursel, "Metrology for Spatial Interferometry I," Proceedings of the SPIE International Symposium on AeroSense, Conference on Spaceborne Interferometry II, vol. 2477, Orlando, FL, April 1995.
10. B. Hines, "Optical Design Issues for the Micro-Precision Interferometer Testbed for Space-Based Interferometry," Proceedings of the SPIE Symposium on OE/Aerospace, Science and Sensing, Conference on Spaceborne Interferometry, vol. 1947, pp. 114-125, Orlando, FL, April 1993.
11. J. W. Melody, H.C. Briggs, "Analysis of Structural and Optical Interactions of the Precision Optical Interferometer In Space (POINTS)," Proceedings of the SPIE Symposium on OE/Aerospace, Science and Sensing, Conference on Spaceborne Interferometry, vol. 1947, pp. 44-57, Orlando, FL, April 1993.
12. J.T. Spanos, Z. Rahman, and G. Blackwood, "A Soft 6-Axis Vibration Isolator," American Controls Conference, Seattle, WA, June 1995.
13. D.W. Miller, S.L. Crawford, T.T. Hyde, G.H. Blackwood, M.M. Colavita, J.W. Yu, "System-wide Design Issues for the Stellar Interferometer Technology Experiment (SITE)," Proceedings of the SPIE International Symposium on AeroSense, Conference on Spaceborne Interferometry II, vol. 2477, Orlando, FL, April 1995.